



Automated Cell Viability Analysis in Tissue Scaffolds

Doku İskelelerinde Otomatik Hücre Canlılığı Analizi

Tansel Uyar^{1,z}, Aykut Erdamar², Menemşe Gümüşderelioğlu¹, Mehmet Fevzi Akşahin²,
Gülseren İrmak^{1,3}, Osman Eroğul⁴

¹Department of Bioengineering, Hacettepe University, Ankara, Turkey.

²Department of Biomedical Engineering, Başkent University, Ankara, Turkey.

³Department of Bioengineering, Turgut Özal University, Malatya, Turkey.

⁴Department of Biomedical Engineering, TOBB University of Economics and Technology, Ankara, Turkey.

ABSTRACT

Image analysis of cell biology and tissue engineering is time-consuming and requires personal expertise. However, evaluation of the results may be subjective. Therefore, computer-based learning and detection applications have been rapidly developed in recent years. In this study, Confocal Laser Scanning Microscope (CLSM) images of the viable pre-osteoblastic mouse MC3T3-E1 cells in 3D bioprinted tissue scaffolds, captured from a bone tissue regeneration study, were analyzed by using image processing techniques. The aim of this study is to develop a reliable and fast algorithm for the automated analysis of live/dead assay CLSM images. Percentages of live and dead cell areas in the scaffolds were determined, and then, total cell viabilities were calculated. Furthermore, manual measurements of four different analysts were obtained to evaluate subjectivity in the analysis. The measurement variations of analysts, also known as the coefficient of variation, were determined from 13.18% to 98.34% for live cell images and from 9.75% to 126.02% for dead cell images. Therefore, an automated algorithm was developed to overcome this subjectivity. The other aim of this study is to determine the depth profile of viable cells in 3D tissue scaffolds. Consequently, cross-sectional image sets of three different types of tissue scaffolds were analyzed.

Key Words

Image correlation; edge detection; cell area counting; tissue engineering.

ÖZ

Hücre biyolojisi ve doku mühendisliğinde görüntü analizi zaman alan ve kişisel uzmanlık gerektiren bir işlemdir. Ancak sonuçların değerlendirilmesi öznel olabilir. Bu nedenle bilgisayar destekli öğrenme ve tespit uygulamaları son yıllarda hızla gelişmiştir. Bu çalışmada, bir kemik dokusu rejenerasyon çalışmasından yakalanan, 3D biyo-baskılı doku iskelelerinde canlı pre-osteoblastik fare MC3T3-E1 hücrelerinin Konfokal Lazer Taramalı Mikroskop (CLSM) görüntüleri, görüntü işleme teknikleri kullanılarak analiz edilmiştir. Bu çalışmanın amacı, canlı/ölü analizi CLSM görüntülerinin otomatik analizi için güvenilir ve hızlı bir algoritma geliştirmektir. İskelelerdeki canlı ve ölü hücre alanlarının yüzdeleri belirlenmiş ve ardından toplam hücre canlılıkları hesaplanmıştır. Ayrıca, analizde özneliği değerlendirmek için dört farklı analistin manuel ölçümleri yapılmıştır. Varyasyon katsayısı olarak da bilinen analistlerin ölçüm varyasyonları, canlı hücre görüntüleri için % 13.18 ile % 98.34 ve ölü hücre görüntüleri için % 9.75 ile % 126.02 arasında belirlenmiştir. Bu nedenle, bu özneliği aşmak için otomatik bir algoritma geliştirilmiştir. Bu çalışmanın diğer amacı, 3 boyutlu doku iskelelerindeki canlı hücrelerin derinlik profilini belirlemektir. Sonuç olarak, üç farklı doku iskelesinin kesitsel görüntü setleri analiz edilmiştir.

Anahtar Kelimeler

Görüntü korelasyonu; Kenar algılama; hücre alanı sayımı; doku mühendisliği.

Article History: Received: Jan 1, 2022; Revised: Apr 2, 2022; Accepted: June 7, 2022; Available Online: Oct 8, 2022.

DOI: <https://doi.org/10.15671/hjbc.868396>

Correspondence to: T. Uyar, Department of Biomedical Engineering, Başkent University, Ankara, Turkey.

E-Mail: tuyar@baskent.edu.tr

INTRODUCTION

Biological images contain patterns, objects and/or living cells that provide functional information about the structure or system being viewed. Some of these images may belong to artificial materials, while others may belong to the culture images of cellular structures. Various imaging techniques such as confocal laser scanning microscopy (CLSM), scanning electron microscopy, and optical microscopy can be used to obtain images of materials or cells [1,2]. These images can be examined using semi-automatic and/or fully-automatic software [3–5]. Many researchers use image analysis programs such as ImageJ to perform manual analysis [6]. Various information about abiotic environments, such as cells and tissue, can be obtained from this software. For example, some tissue scaffold properties such as fiber diameter, pore diameter and permeability can be determined, and also cell and tissue properties such as the amount of cell, percentage of cell viability, area covered by cells can be analyzed [7-20]. There are several approaches to analyze these properties and obtain the analytical data. One of these approaches is user-dependent utilities (Image J, etc). In user-dependent approach, analyses take a very long time and also require personal expertise [21]. Other approaches are semi-automated and fully-automated analysis software which user does not have direct influence. They shorten the analysis time and reduce the dependency on the user. Thus, subjective results derived from the user can be avoided. There are various studies in the literature about automatic approaches [22]. Confocal microscopy images were used to identify glial fibrillary acidic proteins (GFAP) found in brain astrocytes in one of the studies and an algorithm was developed to classify cells [23]. In a similar study, the region of the cell nucleus was identified in an image obtained from mouse hippocampus by staining cell nuclei and RNA in different colors [24]. Piccinini et al. studied optical microscopy images obtained by staining dead cells with trypan blue. These images were analyzed and live and dead cells were classified [25]. In another study, an algorithm was developed to distinguish myelin sheath and nerve itself from the nerve through the SEM images of a nerve bundle. The axons in the inner part of the nerve bundle and the myelin sheaths that surrounding these axons were determined separately and a distribution graph of the diameters of the nerve fibers in the nerve bundle was extracted [26].

In this study, CLSM images obtained from MC3T3-E1

pre-osteoblastic cells (osteoblast precursor) on alginate and alginate-HAp (hydroxyapatite) tissue scaffolds were used. At first, the percentages of the area of the live and dead cells were calculated by four different analysts using ImageJ utility. Then, the developed algorithm was performed semi-automatically for the same analysis and the percentages of the area that belongs to the live and dead cells were calculated. The innovative approach of the developed method is adaptive and calculates the area percentages of the dead cells according to similar studies in the literature. In the presented method, firstly raw images were separated by the pre-processing step. Afterwards, an image correlation algorithm for living cells, and an adaptive statistical approach for dead cells were developed. Then, the results of the algorithm and visual scoring were compared. Moreover, the coefficient variance was calculated to determine the measurement deviation between manual analyses. After the algorithm was successfully developed, cross-sectional CLSM images of live MC3T3-E1 cells in three different tissue scaffolds (alginate-HAp, conventional Gel-MA and microwave-assisted Gel-MA) were analyzed. Using these image sets, it was determined how the viability of the cells changed depending on the depth of the tissue scaffold in further studies. All cross-sectional images were examined, and a percentage of the viability related to depth was calculated. This characterization process is another innovative aspect of this study. The maximum and minimum cell viability was determined as a function of depth.

MATERIALS and METHODS

Production of Tissue Scaffolds

Alginate and Alginate-Hydroxyapatite (HAp) scaffolds

Alginate and alginate-HAp tissue scaffolds were produced by cross-linking reaction. Sodium alginate was dissolved in PBS (pH: 7.4) at a concentration of 3% (w/v). CaSO₄ (1%,w/v) was added into the sodium alginate solution to initiate internal gelation. Then, internal cross-linking was carried out by mixing the two solutions via a three-way valve. The mixing ratios of CaSO₄ and sodium alginate solutions were optimized in terms of printability and gelation. For encapsulation of cells, MC3T3-E1 pre-osteoblasts were dispersed in hydrogels at a density of 3x10⁷ cells/mL. The resulting viscous solution was imprinted in 24-well Petri dishes via Fab@Home bioprinter. As a result of the extruder-based imprinting

process, cell-entrapped constructs in cylindrical geometry (6 mm x 1 mm) were obtained. These constructs were cross-linked with CaCl_2 and transferred to the cell culture stage in the presence of nutrient medium in a CO_2 incubator. The same process was repeated with the addition of the nano-HAp, which was produced by the biomimetic approach [27], into the sodium alginate solution, thus alginate-HAp tissue scaffolds including MC3T3-E1 cells were obtained.

Methacrylated gelatin (Gel-MA) scaffolds

Gelatin was methacrylated by two ways: Conventional method [28] and microwave-assisted methacrylation [29]. The reaction products, conventional Gel-MA and microwave-assisted Gel-MA, were dried in a freeze-dryer (Christ, Germany) and stored at -80°C until hydrogel preparation steps. Methacrylated gelatin (Gel-MA) hydrogels were prepared by photo-crosslinking in the presence of photo-initiator (Irgacure, 0.3 w/v). Irgacure was completely dissolved in PBS (pH: 7.4) at 50°C . Gel-MA was dissolved in this solution at 37°C . MC3T3-E1 mouse pre-osteoblast cells were gently dispersed and mixed into sterile hydrogel solutions at a density of 2×10^7 cells/mL. A cell-bio-ink mixture was loaded into the deposition syringes of Fab@Home bioprinter and printed along the X–Y–Z target paths. After printing, cell-laden hydrogel disks (6 mm x 1 mm) were immediately crosslinked with UV (320–480 nm) light at an intensity of 200 mW/cm^2 for 40 s.

Imaging of Cell Viability

Alginate and alginate-HAp hydrogel scaffolds

In this study, the images that were used for viability analysis were captured by using a confocal laser scanning microscope (Zeiss, LSM510) with a live / dead analysis molecular probe (Life Technology). Images were captured in sequential scanning mode using 0.5, 20x/0.5 and 1 AU values in numerical aperture number, objective magnification (Zeiss Plan-Neofluar objecti-

ve) and pinhole size parameters, respectively. On days 3 and 9 of the culture, cell-containing hydrogels were washed with PBS (pH: 7.4) and incubated with $2 \mu\text{M}$ calcein AM and $4 \mu\text{M}$ ethidium homodimer (EthD-1) before imaging. In this protocol, live cells were stained green with fluorescein marker calcein acetoxymethyl (calcein AM), while dead cells were stained red with EthD-1 [27]. The true color (RGB) images obtained by the aforementioned technique were recorded in a 'tif' image format with a size of 1024×1024 (Real size equivalent in material: $460 \mu\text{m} \times 490 \mu\text{m}$) pixels.

Conventional and microwave-assisted Gel-MA hydrogel scaffolds

The cell viability of these group of hydrogels were examined using a live/dead viability kit. The cell-laden hydrogels were washed in PBS and incubated in $2 \mu\text{M}$ Calcein AM and $4 \mu\text{M}$ ethidium homodimer (Ethd-1) solution for 30 min. The cell-loaded Gel-MA hydrogels were observed under a confocal microscope (Zeiss, LSM 510) with the same parameters that detailed above. Two image sets of 3D bioprinted tissue scaffolds were taken from on day 3.

Image Processing Techniques for Analysis of Live or Dead Cell Percentages

CLSM images were analyzed using MATLAB 2015b. Images used in the study were obtained from pre-osteoblastic MC3T3-E1 cell cultures. In the cell culture study, 35 different images obtained from 3D bioprinted tissue scaffolds were analyzed. Then, 25 cross-sectional images of three different tissue scaffolds at every $9 \mu\text{m}$ were taken from each tissue scaffold for cell viability characterization. This process was carried out to investigate the depth-dependent variation of the cell growth rate in experimental cell culture studies. During characterization, the same algorithm was used to determine viability as the function of depth. The block diagram for the developed algorithm was given in Figure 1.

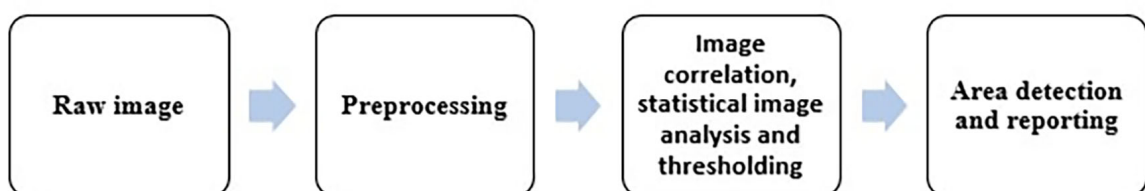


Figure 1. Block diagram of the image analysis algorithm.

Preprocessing

The following algorithm steps were applied to the cell images in the preprocessing part.

Splitting RGB image into layers: RGB image consists of three layers which are red, green, and blue channels. Based on the current staining technique, a green layer for the live cell and a red layer for the dead cell were obtained from the RGB image [27]. In splitting process, overlapped regions were excluded owing to the uncertainty about viability condition.

Removing noises from the image: The noise on the images which was caused by the imaging technique was removed using Wiener adaptive filter. This filter is an effective tool for removing signal-independent zero-mean white Gaussian noise [30]. Noisy image can be modeled as in Eq.1.

$$x_{i,j} = y_{i,j} + n_{i,j} \quad (1)$$

$x_{i,j}$ is the noisy image, $y_{i,j}$ is the noise-free image and $n_{i,j}$ is the additive Gaussian noise. The aim of the noise removal process is to suppress the noise stemming from noisy image ($x_{i,j}$) by minimizing the mean squared error (MSE). A linear estimate $\hat{y}_{i,j}$ of $y_{i,j}$ is derived from Eq.2 where N is the number of elements in $y_{i,j}$. At this point, Wiener filter minimizes the mean square error between the estimated image $\hat{y}_{i,j}$ and the original image $y_{i,j}$ in Eq.2 [31].

$$MSE(\hat{y}) = \frac{1}{N} \sum_{i,j=1}^N (\hat{y}_{i,j} - y_{i,j})^2 \quad (2)$$

$x_{k,l}$ is the density value of a pixel in the NxN image. Pixel-wise adaptive Wiener filter use neighborhoods of size $(2n+1) \times (2m+1)$ window to estimate the local image mean and standard deviation. In this study, window size was chosen as 5×5 [32]. It assumes that the noise is stationary with zero mean and variance $\sigma_{i,j}$ and uncorrelated with the original image $x_{k,l}$. Based on these assumptions, Wiener adaptive filter estimates the local mean and variance around each pixel using Eq.3 and Eq.4 [32–34]. If the variance is large, the Wiener filter performs little smoothing. If the variance is small, the Wiener filter performs more smoothing.

$$m_{i,j} = \frac{1}{(2n+1)(2m+1)} \sum_{k=i-n}^{i+n} \sum_{l=j-m}^{j+m} x_{k,l} \quad (3)$$

$$\sigma_{i,j} = \frac{1}{(2n+1)(2m+1)} \sum_{k=i-n}^{i+n} \sum_{l=j-m}^{j+m} (x_{k,l} - m_{i,j})^2 \quad (4)$$

$$x'_{i,j} = m_{i,j} + \frac{\sigma_{i,j} - v_{i,j}}{\sigma_{i,j}} (x_{i,j} - m_{i,j})$$

$m_{i,j}$ is the local mean in Eq.3 and $\sigma_{i,j}$ is the local variance in Eq.4. Then Wiener filter creates a pixel-wise filtering using these estimates and estimated image is obtained according to Eq.5.

$$x'_{i,j} = m_{i,j} + \frac{\sigma_{i,j} - v_{i,j}}{\sigma_{i,j}} (x_{i,j} - m_{i,j}) \quad (5)$$

$v_{i,j}$ is the local noise variance in Eq.5, was obtained using the mean value of all local estimated variances [32–34].

Smoothing the image with Gaussian filter: After the noise removal step, Gaussian type low-pass filter was applied to fill tiny gaps in cells and to remove high frequency noise. Most edge-detection algorithms are sensitive to noise [35]. This filtering was used because of the edge-detection in the next part. Gaussian matrix (h_g) was generated with 5×5 kernel size due to $\sigma=1$ standard deviation in Eq.6 [36]. Gaussian matrix formed in before was convolved with image according to Eq.7 and new softened image (h) was obtained.

$$h_g(n_1, n_2) = e^{-\frac{(n_1^2 + n_2^2)}{2\sigma^2}} \quad (6)$$

$$h(n_1, n_2) = \frac{h_g(n_1, n_2)}{\sum_{n_1} \sum_{n_2} h_g} \quad (7)$$

Image correlation, statistical image analysis and thresholding process

In order to obtain live cells contour on the preprocessed image cross-correlation, statistical image analysis and then thresholding steps were performed. Two dimensional cross-correlation function was calculated with Eq.8. X is the MxN sized preprocessed image and H is the PxQ sized template which was selected as a mask in Eq.8. Template was selected in based on pixel size to cover the whole cell. For this reason, P and Q values may change according to the size of the template. At the end of this process, the correlation matrix was obtained in (N+Q-1) x (M+P-1) dimensions [37].

$$C(k,l) = \sum_{m=0}^{M-1-N-1} \sum_{n=0}^{N-1-Q-1} X(m,n) \bar{H}(m-k,n-l)$$

$$-(P-1) \leq k \leq M-1,$$

$$-(Q-1) \leq l \leq N-1,$$
(8)

Afterwards, normalization process was performed to the correlated image by using Eq. 9. Where, X' is the normalized cross-correlation matrix, μ is the mean of the cross-correlation matrix and σ is the standard deviation of the cross-correlation matrix.

$$X' = \frac{X - \mu}{\sigma}$$
(9)

In the normalization process, the average pixel value of the image was subtracted from each pixel value and the calculated difference was divided by the standard deviation. With this process live cells were identified by positive values. Also, non-viable regions were identified by negative values. Owing to this situation, the threshold value has been set to zero.

Then, edge detection functions were used to extract contours from the thresholded image. For edge detection process, three different algorithms (Sobel, Prewitt and Canny) were applied [37]. For the edge detection process, Sobel kernels in Figure 2a, Prewitt kernels in Figure 2b and Canny kernels in Figure 2c were used for convolution.

In order to minimize the methodological error, three methods were separately used. Then three edge detected images were combined with each other by adding one image. The final edge detected image was superimposed on the raw image.

Adaptive thresholding for dead cells: The thresholding method for living cells has been insufficient for the detection of dead cells. Therefore, a different approach has been developed. In this approach, threshold values for detecting dead cells were obtained adaptively from the images. These threshold values were determined using the statistical analysis of the pixel density histograms of dead cell images. Accordingly, two threshold levels were designated for adaptive thresholding based on dead cell images. is the value obtained by dividing the average values of the image matrix by the standard deviation of the matrix values (Eq.10) and is the average value of the image matrix (Eq.11).

$$threshold1 = \left| \frac{mean(matrix)}{standartdeviation(matrix)} \right|$$
(10)

$$threshold2 = |mean(matrix)|$$
(11)

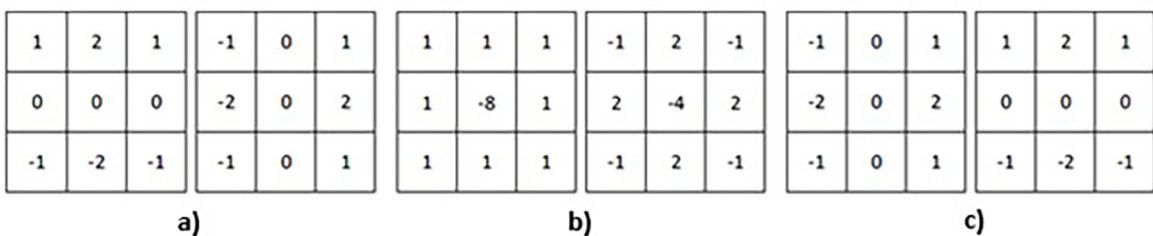


Figure 2. Edge detection kernels used for convolution, a) Sobel kernels, b) Prewitt kernels, c) Canny kernels.

After these threshold values were calculated, the median values of intensity levels in each line of the image were selected for each row and they were obtained as an one-dimensional vector. The highest value of this vector was selected as a selector for the adaptive thresholding. This value was used for threshold selection. The operation used in the algorithm was explained as a conditional expression in Eq.12.

$$\begin{aligned} \text{If } \text{maximumvalue}_{\text{median}} \geq \text{threshold2} & \Rightarrow \text{use threshold1;} \\ \text{If } \text{maximumvalue}_{\text{median}} < \text{threshold2} & \Rightarrow \text{use threshold2;} \end{aligned} \quad (12)$$

Once the threshold value has been selected, dead-cell areas were detected by applying an image thresholding

process. After cell lines were identified, dead cell contours were determined with the edge detection method that was explained in advance. Then cell contour image was placed on the gray level image of dead cells.

Detection of cell area and calculation

Calculation of live and dead cell percentages

According to the thresholding process, pixel densities higher than the threshold were set to '1' and the others were set to '0'. On the thresholded images of live and dead cells, cell areas were calculated by counting the values of '1's on image with pixel² unit. Percentages of cell areas were calculated by dividing the whole pixel on image into cell areas. After the counting process, the area percentages of the cells were reported.

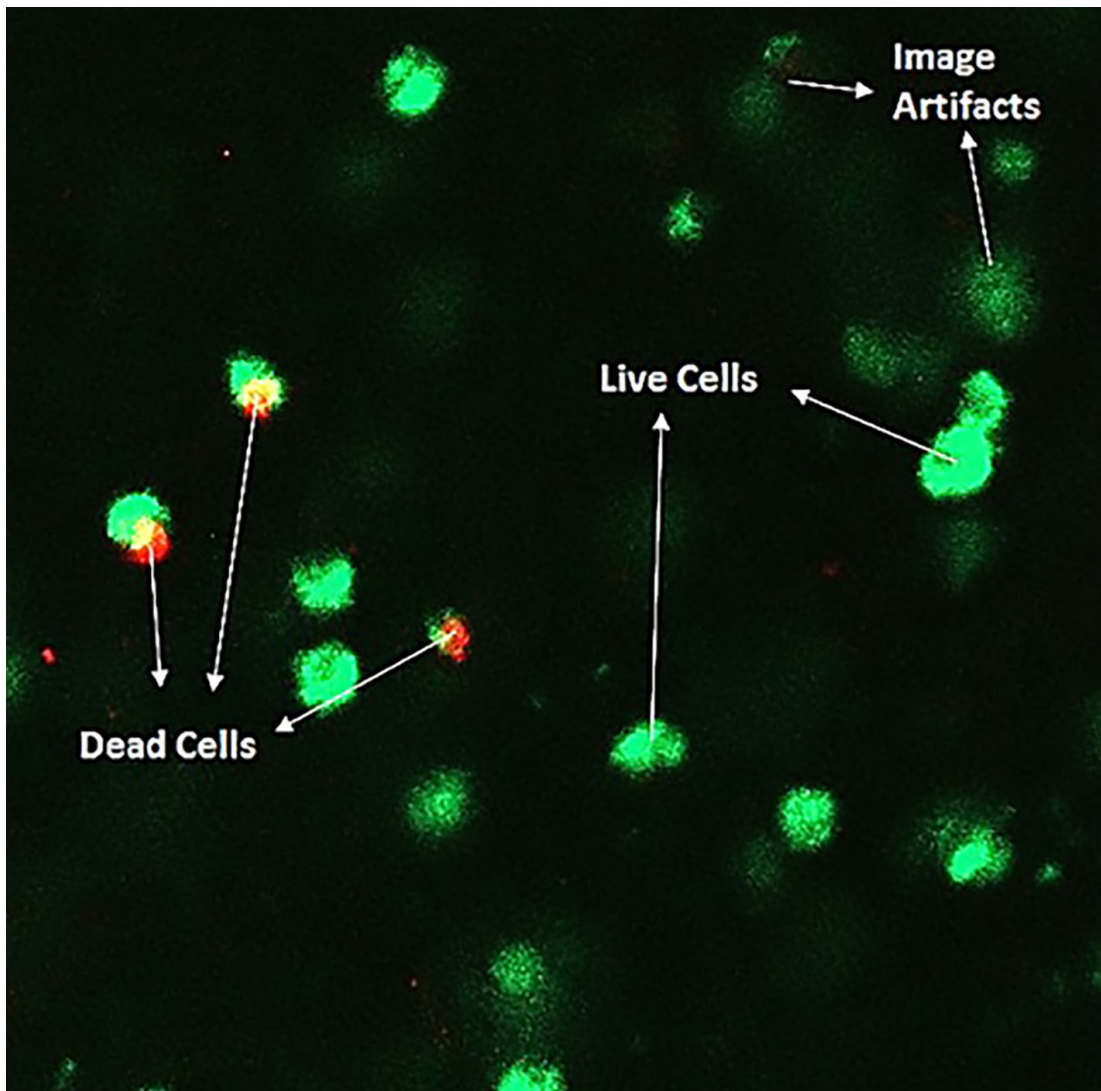


Figure 3. An example of a raw image (3D bioprinted tissue scaffold of alginate-HAp on day 3, Surface image).

Inspection of analysts and reporting of live and dead cell percentages

Images of live and dead cells were analyzed with ImageJ program by four analysts. Each analyst reported his/her measurements and according to these measurements, some of the statistical parameters have been calculated. In this evaluation, average values of calculations, standard deviations and variation coefficient percentages of the numerical values were calculated by the analysts. The variation coefficients, calculated by the mean value ratio of the standard deviation, express how much the distributions in the manual measurements change with respect to the average. The percentage of variation coefficient is the measure of how different analyst are deviating from the average measured value for the same measurement. In other words, it can be described as subjectivity in measurement. Thence, the metrics of the analysts were reported in Experimental Results part.

RESULTS and DISCUSSION

A raw image sample was given in Figure 3. According to the assay protocol, the live cells stained green with calcein AM and the locations of the dead cells stained red with EthD-1 were shown in the Figure 3. Non-cell image artifacts, which produce fluorescence effect by interacting with HAp in the tissue scaffold, were also indicated in this raw image (Figure 3).

In the preprocessing step, firstly the raw image was divided into red, green and blue layers so that dead and living cells can be analyzed separately. In addition, the overlapping parts of the living and dead cells in the red and green layers were also removed to prevent mistakes that may be caused by the dyeing technique or the imaging technique. Then, the Wiener adaptive noise filter was applied to the images. As the last step of preprocessing, Gaussian type low pass filter was applied to soften the images. The images obtained as a result of the preprocessing steps were given in Figure 4.

After the preprocessing step of the algorithm, the green and red image layers were converted to gray level. Correlation, normalization, and thresholding steps were performed for live cells as described in Image correlation, statistical analysis and thresholding section. For dead cells, as described in Image correlation, statistical analysis and thresholding section, an adaptive threshold value derived from images containing dead cells and varying with each image was used. Eventually, the contours of the live and dead cells in the images were determined and the superimposed-on images obtained as a result of preprocessing, and they were converted to gray level (Figure 5).

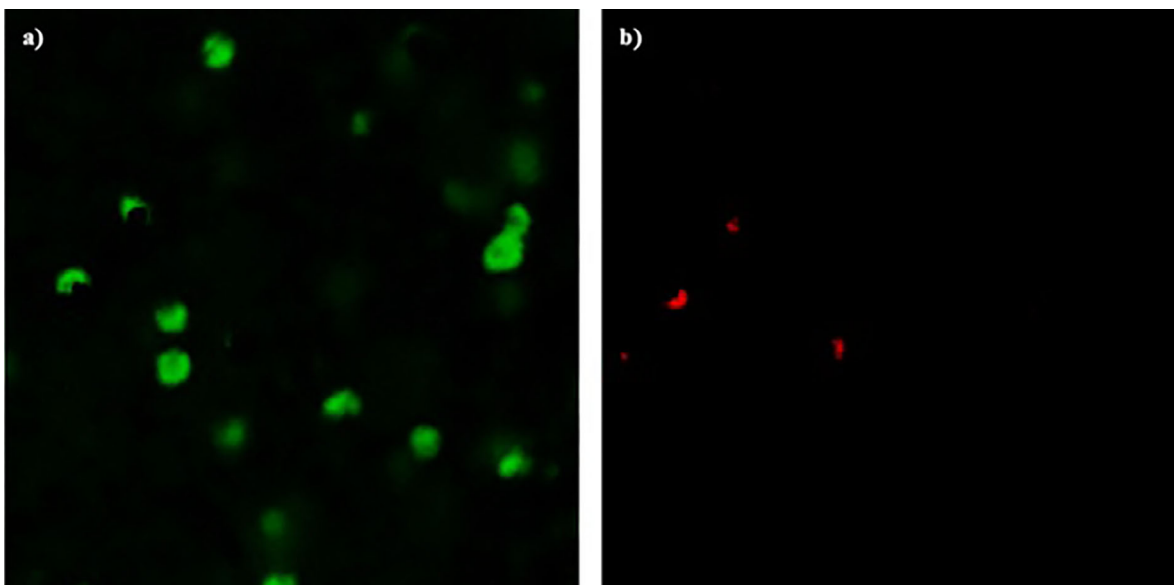


Figure 4. Images obtained as a result of preprocessing steps, a) Live cells, b) Dead cells.

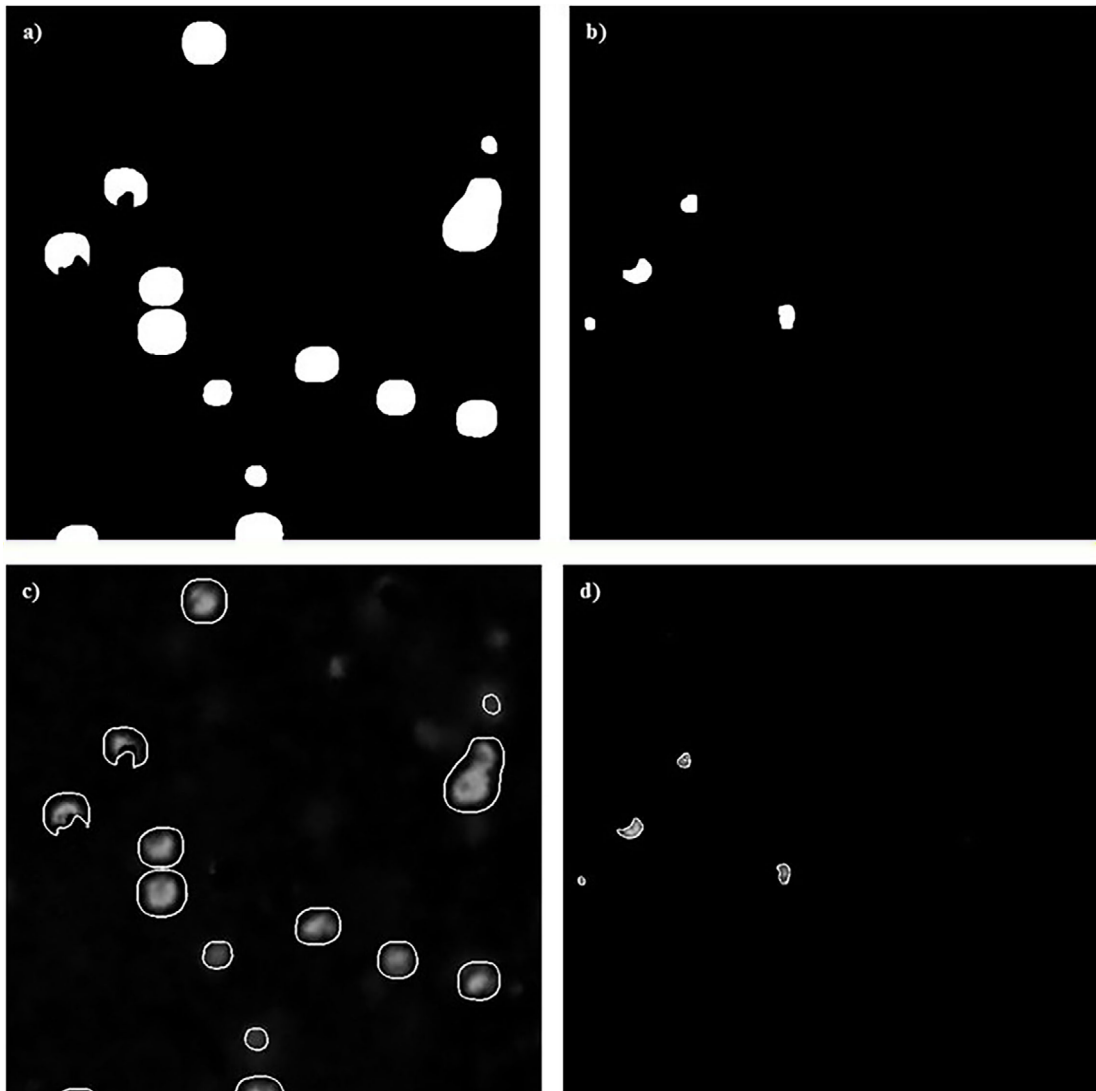


Figure 5. Images obtained as a result of thresholding and edge detection process, a-c) Live cells, b-d) Dead cells.

Thirty-five CLSM images of alginate and alginate-HAP tissue scaffolds were analyzed using the developed algorithm and live and dead cell percentages were calculated. In addition, the same image set was analyzed manually by four different analysts with ImageJ mentioned in Detection of cell area and calculation section. The results acquired from the algorithm were evaluated on the basis of analysts' results and statistical analysis. The measurements and calculations for image the set were given in Table 1.

As a result of this calculation process; intervals of variation coefficient percentages were obtained and average values of variation coefficient percentages were calculated (Table 2).

The other goal of this study is to determine the cell viability depending on the depth of the tissue scaffold. For this purpose, the change in the viability percentages of MC3T3-E1 cells in tissue scaffolds was investigated based on the depth of the tissue scaffold. For this characterization, the MC3T3-E1 cells implanted into the produced three different tissue scaffolds (alginate-HAP, traditional gel-MA, and microwaved gel-MA) were visualized with CLSM. Cross-section images were taken at every 9 μm and an image set was created for each tissue scaffold with 25 individual cross-sectional image. Each cross-sectional image in this set was examined separately and the viability percentages of the cross-sectional areas were calculated. The percentage of the live cell area depending on the depth of the tissue scaffolds was shown in Figure 6.

Table 1. Calculations for the image set (The variables given in the table are A1: Analyst 1, A2: Analyst 2, A3: Analyst 3, A4: Analyst 4, MA = Mean of Analysts, ASD = Standard Deviation of Analysts, AL: Algorithm Result, VC = Percentage of Variation Coefficient, CC: Cell Condition, LCI=Live Cell Image, DCI=Dead Cell Image, Calculation of all measurements are given in percentages).

Image No.	CC	A1%	A2%	A3%	A4%	MA%	SD	VC%	AL%
1	LCI	3.228	4.277	4.034	5.863	4.351	0.956	21.97	4.740
	DCI	0.205	0.246	0.318	0.420	0.297	0.081	27.40	0.394
2	LCI	3.335	3.613	3.387	5.332	3.917	0.824	21.03	4.156
	DCI	0.277	0.756	0.491	0.041	0.391	0.264	67.47	0.301
3	LCI	3.922	6.554	6.76	13.971	7.802	3.733	47.85	6.336
	DCI	0.254	0.331	0.572	0.439	0.399	0.120	29.96	0.219
4	LCI	5.037	3.648	4.189	5.668	4.635	0.775	16.72	4.936
	DCI	0.343	0.227	0.673	0.230	0.368	0.182	49.47	0.142
5	LCI	4.438	7.670	6.146	4.531	5.696	1.327	23.29	5.883
	DCI	0.202	0.658	0.522	0.124	0.376	0.221	58.64	0.122
6	LCI	5.649	6.351	8.107	11.235	7.835	2.157	27.53	7.201
	DCI	0.538	0.658	1.457	0.311	0.741	0.432	58.25	0.620
7	LCI	2.234	3.837	4.592	12.415	5.770	3.930	68.12	6.896
	DCI	0.105	0.114	0.251	1.175	0.411	0.445	108.13	0.432
8	LCI	6.028	7.669	10.801	8.848	8.337	1.740	20.87	6.767
	DCI	0.357	0.249	1.213	0.066	0.471	0.441	93.51	0.306
9	LCI	3.804	3.858	8.435	12.584	7.170	3.647	50.87	8.238
	DCI	0.021	0.060	0.659	0.878	0.404	0.372	92.06	0.137
10	LCI	5.028	6.489	10.361	7.683	7.390	1.956	26.47	7.770
	DCI	0.5	0.328	0.827	0.061	0.429	0.278	64.78	0.288
11	LCI	2.402	3.273	2.811	11.208	4.924	3.641	73.96	6.051
	DCI	0.167	0.163	0.277	0.838	0.361	0.279	77.23	0.581
12	LCI	1.238	1.566	2.033	3.561	2.100	0.890	42.39	3.340
	DCI	0.083	0.166	0.158	0.143	0.138	0.033	23.65	0.059
13	LCI	1.543	2.740	2.871	2.030	2.296	0.540	23.51	3.347
	DCI	0.233	0.193	0.348	0.108	0.221	0.086	39.10	0.166
14	LCI	2.453	3.526	3.064	3.358	3.100	0.409	13.18	4.362
	DCI	0.501	0.878	0.381	0.188	0.487	0.252	51.68	0.215
15	LCI	1.155	1.212	0.848	1.546	1.190	0.248	20.81	1.614
	DCI	0.099	0.217	0.206	0.300	0.206	0.071	34.76	0.094
16	LCI	1.165	2.697	3.173	3.540	2.644	0.905	34.21	2.354
	DCI	0.373	0.147	0.391	0.513	0.356	0.132	37.12	0.429
17	LCI	3.814	3.090	4.776	5.230	4.228	0.832	19.69	5.024
	DCI	0.145	0.401	0.386	0.235	0.292	0.107	36.59	0.259
18	LCI	4.202	4.817	6.591	6.726	5.584	1.097	19.65	5.957
	DCI	0.109	0.063	0.232	0.323	0.182	0.102	56.29	0.044
19	LCI	3.685	3.729	4.874	3.324	3.903	0.582	14.92	4.533
	DCI	0.217	0.225	0.839	0.921	0.551	0.331	60.09	0.832
20	LCI	4.128	3.031	5.111	6.279	4.637	1.200	25.88	4.962
	DCI	0.105	0.225	0.383	0.264	0.244	0.099	40.63	0.134

Table 1. Continue.

Image No.	CC	A1%	A2%	A3%	A4%	MA%	SD	VC%	AL%
21	LCI	1.948	4.002	3.126	5.632	3.677	1.344	36.54	3.915
	DCI	0.115	0.100	0.334	0.236	0.196	0.095	48.62	0.322
22	LCI	3.028	4.981	2.981	5.863	4.213	1.249	29.63	4.740
	DCI	0.251	0.202	0.423	0.516	0.348	0.127	36.51	0.394
23	LCI	1.162	1.212	2.903	2.236	1.878	0.731	38.90	2.532
	DCI	0.122	0.571	0.302	0.782	0.444	0.252	56.75	0.179
24	LCI	10.666	10.997	12.548	16.502	12.678	2.319	18.29	10.279
	DCI	0.2	0.252	0.2	0.221	0.218	0.021	9.75	0.091
25	LCI	2.048	4.351	5.755	12.731	6.221	3.985	64.047	7.711
	DCI	0.203	0.145	0.203	0.476	0.257	0.129	50.166	0.000
26	LCI	6.657	5.187	12.197	7.388	7.857	2.628	33.446	6.282
	DCI	1.545	1.142	2.279	2.252	1.804	0.483	26.743	0.058
27	LCI	4.236	4.021	7.349	10.574	6.545	2.673	40.843	7.320
	DCI	0.964	0.140	3.933	0.000	1.259	1.587	126.029	0.657
28	LCI	3.598	2.651	4.960	9.390	5.150	2.582	50.140	6.453
	DCI	0.833	0.894	2.993	1.557	1.569	0.870	55.417	0.504
29	LCI	4.980	2.412	7.827	7.308	5.632	2.146	38.105	5.546
	DCI	0.539	0.104	4.008	0.695	1.337	1.557	116.525	2.230
30	LCI	1.576	1.529	6.760	6.340	4.051	2.503	61.789	6.530
	DCI	0.555	0.471	1.495	0.245	0.691	0.478	69.066	2.234
31	LCI	1.220	0.570	7.190	5.046	3.507	2.729	77.826	6.527
	DCI	0.109	0.375	0.435	0.183	0.276	0.134	48.558	0.018
32	LCI	2.137	3.310	11.083	2.444	4.744	3.685	77.688	4.727
	DCI	0.103	0.145	0.843	0.587	0.420	0.309	73.751	0.000
33	LCI	0.816	0.626	3.326	9.023	3.448	3.390	98.342	5.751
	DCI	0.333	0.086	0.527	0.156	0.275	0.171	62.055	0.911
34	LCI	0.581	0.478	4.302	3.563	2.231	1.722	77.177	3.484
	DCI	0.034	0.031	0.109	0.229	0.101	0.080	79.672	0.511
35	LCI	1.922	2.021	7.878	2.500	3.580	2.491	69.573	2.471
	DCI	0.153	0.196	1.500	0.372	0.555	0.552	99.345	0.651

Table 2. Statistical analysis of analysts' measurements results.

Glycerol Concentrations (%)	Intervals of Variation Coefficient Percentages (%)	Average Values of Variation Coefficient Percentages (%)
Live Cell Images	13.18 - 98.34	40.72
Dead Cell Images	9.75 - 126.02	59.02

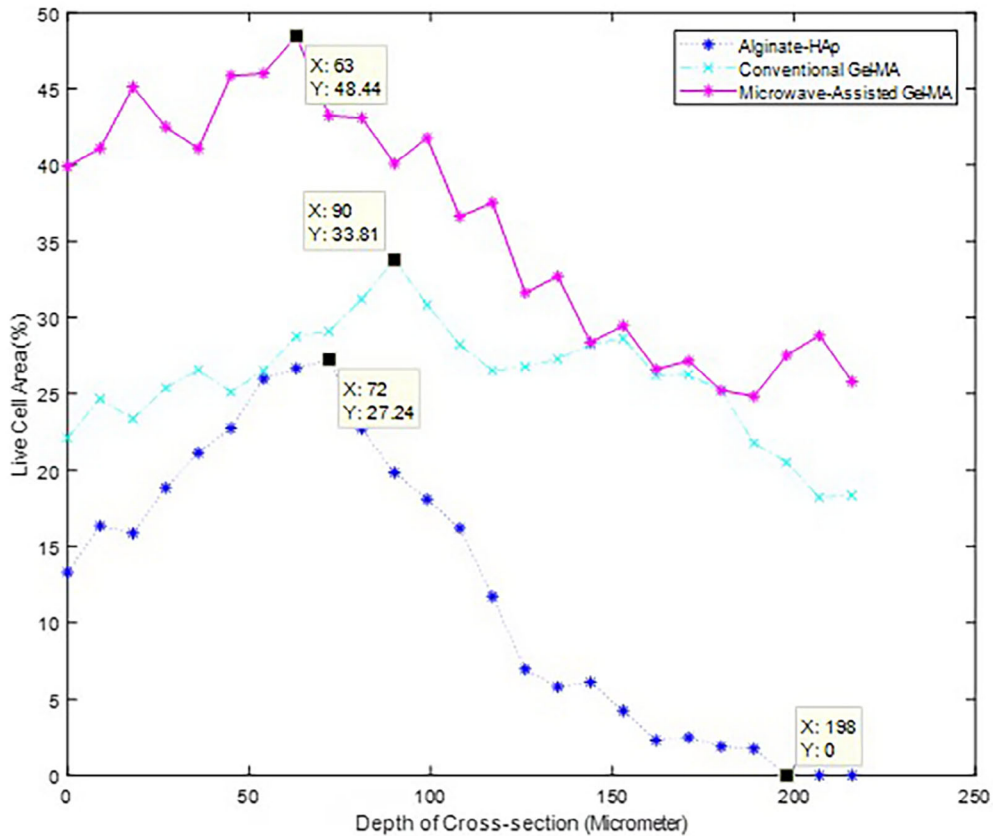


Figure 6. Cell viability change depending on the depth of tissue scaffolds.

Maximum cell viabilities were obtained down from the tissue scaffold at intervals of 63 μm and 90 μm . Maximum cell viability of Alginate-HAp was obtained at 72 μm and viability of the cells rapidly decreased until 198 μm . After this depth, there was no viability observed. For Traditional Gel-MA and Microwaved Gel-MA, the maximum cell viabilities were obtained at 90 μm and 63 μm , respectively. After these points, viability of cell rapidly decreased but never reached zero for either tissue scaffolds. Three images of maximum cell viability for tissue scaffolds were shown in Figure 7.

DISCUSSION

In this work, study was designed to semi-automatically detect cell viability based on the depth of the 3D bioprinted tissue scaffold. Firstly, an algorithm has been developed which enables accurate detection of live and dead cells. The algorithm can easily distinguish separate

cells. However, it may be insufficient to distinguish adjacent intertwined cells in some cases. To overcome this problem, detected cell areas were used instead of cell number in calculations. In this way, a relative cell viability evaluation can be made. In the continuation of the study, the cell viability in the 3D bioprinted tissue scaffold was determined depending on the depth. Contrary to the studies frequently encountered in the literature, in which the scaffold material structure was examined in the 3D plane, the efficiency of cell activity was examined in the 3D plane in the presented study [22,28,39]. In this study, the examination of cell activity, which changes due to different material properties, along the 3d section plane, constitutes its distinguishing aspect from other material-cell interaction studies in the literature [22,29,40]. However, unlike the manual evaluations performed with user-based software in the literature for cell detection, in the presented study, multiple evaluations could be made in a short time with a semi-automatically

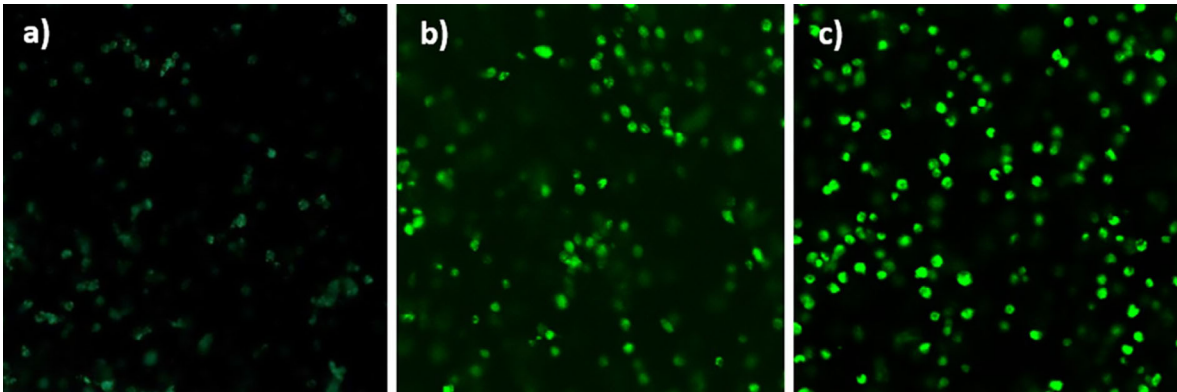


Figure 7. Depth images of tissue scaffolds with the highest percentage of cell viability, a) Alginate-HAp (72 μm) b) Conventional Gel-MA (90 μm) c) Microwave-assisted Gel-MA (63 μm).

tic software design that is least dependent on the user (analyst) [41]. At this point, user reliability, which is another perspective of the study, is also discussed in order to make user (analyst) and software comparisons. The reliability of the analysis in such studies depends on the segmentation accuracy of live and dead cells. Analysts who are experts in their fields inspect these cell images with a visual examination. Visual inspection may cause subjective results and affect the outcome of the study [6,38]. Furthermore, these results are not reproducible because of the personal expertise of the analysts. One of the goals of this study is to evaluate the results of a person-to-person variation (analyst effect) in the visual analysis. The results of our study showed that analysts may make different interpretations in the examination. These subjective interpretations can cause faulty evaluations that may lead researchers to mislead in their studies. The obtained results were compared with the percentage of the variation coefficient, which represents the measurement difference between four different analysts. The coefficients of the variation were obtained from 13.18 % to 98.34 % for live cells and from 9.75% to 126.02% for dead cells with respect to measurements of the analysts. In addition, the average values of variation coefficient percentages are 40.72% for live cell images and 59.02% for dead cell images. These results indicate the inter-analysts' variabilities. It is thought that the reason for this difference is that the perception of human eyes differs from each other during visual evaluation. Another reason for the high rate of deviation in dead cell images is that the number of cells in the dead cell images is small compared to that of live cell images, and this increases the rate of mis-detection. Also, it is determined that the mean values of the analysts' measurements were close to algorithm

results when Table 1 was examined. In cases where the coefficient of the variation in manual measures is low, the algorithm results are converging the average of the manual results.

CONCLUSIONS

In the study, area percentages of live and dead cells in CLSM images of cell cultures that were implanted to alginate and alginate-HAp tissue scaffolds were calculated semi-automatically. The results show that there were too many deviations between the manual evaluations of the analysts. Conversely, it has been shown that reproducible results can be obtained with the developed algorithm. Moreover, depth-dependent cell viability analyses were performed on the tissue scaffold. The maximum cell viability was obtained at 63 μm , 72 μm and 90 μm for microwave-assisted Gel-MA, alginate-HAp, conventional Gel-MA scaffolds, respectively. For Alginate-HAp scaffold cell viability began to decrease and there was no viability deeper than 198 μm . For conventional Gel-MA and Microwave-assisted Gel-MA tissue scaffolds, cell viability began to decrease but never reached zero percentage. Depending on the depth of the tissue scaffold, a reduction in viability is expected. This situation can be explained by the reduced transport of the nutrition substances needed by the cells based on diffusion physics.

References

1. V. Ntziachristos, Fluorescence Molecular Imaging, *Annu. Rev. Biomed. Eng.*, 8 (2006) 1–33.
2. G.Y. Wiederschain, *The Molecular Probes handbook A guide to fluorescent probes and labeling technologies*, 11th ed., Thermo Fisher Scientific, 2010.
3. W. Grootjans, E.A. Usmanij, W.J.G. Oyen, E.H.F.M. van der Heijden, E.P. Visser, D. Visvikis, M. Hatt, J. Bussink, L.F. de Geus-Oei, Performance of automatic image segmentation algorithms for calculating total lesion glycolysis for early response monitoring in non-small cell lung cancer patients during concomitant chemoradiotherapyFDG-PET in early NSCLC response assessment, *Radiother. Oncol.*, 119 (2016) 473–479.
4. Y. Liu, Y. Chen, B. Han, Y. Zhang, X. Zhang, Y. Su, Fully automatic Breast ultrasound image segmentation based on fuzzy cellular automata framework, *Biomed. Signal Process. Control*, 40 (2018) 433–442.
5. X. Li, J. Liu, Z. Liu, X. He, C. Zhang, H. Yuan, F. Liu, C. Zheng, Automatic detection of leukocytes for cytometry with color decomposition, *Optik (Stuttg.)*, 127 (2016) 11901–11910.
6. G. Narayanan, M.Y. Tekbudak, Y. Caydamli, J. Dong, W.E. Krause, Accuracy of electrospun fiber diameters: The importance of sampling and person-to-person variation, *Polym. Test.*, 61 (2017) 240–248.
7. S. Nazlibilek, D. Karacor, T. Ercan, M.H. Sazli, O. Kalender, Y. Ege, Automatic segmentation, counting, size determination and classification of white blood cells, *Meas. J. Int. Meas. Confed.*, 55 (2014) 58–65.
8. J. Malašauskiene, R. Milašius, Investigation and estimation of structure of web from electrospun nanofibres, *J. Nanomater.*, 2013 (2013).
9. F. Brun, G. Turco, A. Accardo, S. Paoletti, Automated quantitative characterization of alginate/hydroxyapatite bone tissue engineering scaffolds by means of micro-CT image analysis, *J. Mater. Sci. Mater. Med.*, 22 (2011) 2617–2629.
10. H. Ramoser, V. Laurain, H. Bischof, R. Ecker, Leukocyte segmentation and classification in blood-smear images, *Annu. Int. Conf. IEEE Eng. Med. Biol. Soc.*, 4 (2005) 3371–3374.
11. N. Guo, L. Zeng, Q. Wu, A method based on multispectral imaging technique for White Blood Cell segmentation, *Comput. Biol. Med.*, 37 (2007) 70–76.
12. C. Di Ruberto, A. Dempster, S. Khan, B. Jarra, Analysis of infected blood cell images using morphological operators, *Image Vis. Comput.*, 20 (2002) 133–146.
13. Q. Liao, Y. Deng, An accurate segmentation method for white blood cell images, *Proc. - Int. Symp. Biomed. Imaging*, (2002) 245–248.
14. S.H. Rezaatfighi, H. Soltanian-Zadeh, Automatic recognition of five types of white blood cells in peripheral blood, *Comput. Med. Imaging Graph.*, 35 (2011) 333–343.
15. Ö. Kasım, A.E. Kuzucuoğlu, Lökosit hücrelerinin preparat görüntüsünden tespiti ve sınıflandırılması, *Gazi Üniv. Müh. Mim. Fak. Der.*, 30 (2015) 95–109.
16. N. Dehghan, M.A. Tavanaie, P. Payvandy, Morphology study of nanofibers produced by extraction from polymer blend fibers using image processing, *Korean J. Chem. Eng.*, 32 (2015) 1928–1937.
17. E.S. Gelsema, Application of the Method of Multiple Thresholding to White Blood Cell Classification, *Comput. Biol. Med.*, 18 (1988) 65–74.
18. L. Zhao, K. Li, M. Wang, J. Yin, E. Zhu, C. Wu, S. Wang, C. Zhu, Automatic cytoplasm and nuclei segmentation for color cervical smear image using an efficient gap-search MRF, *Comput. Biol. Med.*, 71 (2016) 46–56.
19. X. Bai, P. Wang, C. Sun, Y. Zhang, F. Zhou, C. Meng, Finding splitting lines for touching cell nuclei with a shortest path algorithm, *Comput. Biol. Med.*, 63 (2015) 277–286.
20. D. Yu, T.D. Pham, X. Zhou, Analysis and recognition of touching cell images based on morphological structures, *Comput. Biol. Med.*, 39 (2009) 27–39.
21. J.J. Stanger, N. Tucker, N. Buunk, Y.B. Truong, A comparison of automated and manual techniques for measurement of electrospun fibre diameter, *Polym. Test.*, 40 (2014) 4–12.
22. H. Shen, A.S. Goldstein, G. Wang, *Biomedical Imaging and Image Processing in Tissue Engineering*, in: N. Pallua, C. V. Suschek (Eds.), *Tissue Eng. From Lab to Clin.*, 1st ed., Springer-Verlag Berlin Heidelberg, New York, 2011: pp. 155–178.
23. P.M. Kulkarni, E. Barton, M. Savelonas, R. Padmanabhan, Y. Lu, K. Trett, W. Shain, J.L. Leasure, B. Roysam, Quantitative 3-D analysis of GFAP labeled astrocytes from fluorescence confocal images, *J. Neurosci. Methods*, 246 (2015) 38–51.
24. G. Lin, U. Adiga, K. Olson, J.F. Guzowski, C.A. Barnes, B. Roysam, A hybrid 3D watershed algorithm incorporating gradient cues and object models for automatic segmentation of nuclei in confocal image stacks, *Cytometry*, 56A (2003) 23–36.
25. F. Piccinini, A. Tesei, G. Paganelli, W. Zoli, A. Bevilacqua, Improving reliability of live/dead cell counting through automated image mosaicing, *Comput. Methods Programs Biomed.*, 117 (2014) 448–463.
26. H.L. More, J. Chen, E. Gibson, J.M. Donelan, M.F. Beg, A semi-automated method for identifying and measuring myelinated nerve fibers in scanning electron microscope images, *J. Neurosci. Methods*, 201 (2011) 149–158.
27. T.T. Demirtaş, G. Kaynak, M. Gumuşderelioğlu, Bone-like hydroxyapatite precipitated from 10×SBF-like solution by microwave irradiation, *Mater. Sci. Eng. C*, 49 (2015) 713–719.
28. A.I. Van Den Bulcke, B. Bogdanov, N. De Rooze, E.H. Schacht, M. Cornelissen, H. Berghmans, Structural and rheological properties of methacrylamide modified gelatin hydrogels, *Biomacromolecules*, 1 (2000) 31–38.
29. G. Irmak, T.T. Demirtaş, M. Gumuşderelioğlu, Highly Methacrylated Gelatin Bioink for Bone Tissue Engineering, *ACS Biomater. Sci. Eng.*, 5 (2019) 831–845.
30. F. Jin, P. Fieguth, L. Winger, E. Jernigan, Adaptive Wiener filtering of noisy images and image sequences, in: *Proc. 2003 Int. Conf. Image Process. (Cat. No.03CH37429)*, IEEE, 2003: pp. III-349–52.
31. P. Shukla, A. Boyat, Image Denoising using Local Adaptive Wiener Filter in Spatial and Temporal Domain, *Int. J. Adv. Res. Electron. Commun. Eng.*, 4 (2015) 2019–2024.
32. J. Sen Lee, Digital Image Enhancement and Noise Filtering by Use of Local Statistics, *IEEE Trans. Pattern Anal. Mach. Intell.*, PAMI-2 (1980) 165–168.
33. J.S. Lim, *Two-Dimensional Signal and Image Processing*, 1st ed., Printice Hall, Englewood Cliffs, New Jersey, 1990.
34. J.S. Lee, Refined filtering of image noise using local statistic, *Comput. Graph. Image Process.*, 24 (1983) 255–269.
35. M.S. Nixon, A.S. Aguado, *Feature Extraction & Image Processing for Computer Vision*, 3rd ed., Elsevier Inc., London, 2012.

36. M.P. Wand, C.M. Jones, Kernel Smoothing, First Edit, Chapman & Hall, New York, 1995.
37. R. Gonzalez, R. Woods, B. Masters, Digital Image Processing, Third Edition, Third Edit, Upper Saddle River, New Jersey, 2007.
38. M. Bizrah, S.C. Dakin, L. Guo, F. Rahman, M. Parnell, E. Normando, S. Nizari, B. Davis, A. Younis, M.F. Cordeiro, A semi-automated technique for labeling and counting of apoptosing retinal cells, BMC Bioinformatics, 15 (2014) 169.
39. A.M. Abd El-Aziz, A. El-Maghraby, A. Ewald, S.H. Kandil, In-vitro cytotoxicity study: cell viability and cell morphology of carbon nanofibrous scaffold/hydroxyapatite nanocomposites, Molecules, 26 (2021) 1552.
40. R. Dittmar, E. Potier, M.v. Zandvoor, K. Ito, Assessment of Cell Viability in Three-Dimensional Scaffolds Using Cellular Auto-Fluorescence, Tissue Engineering: Part C, 18 (2012) 198-204.
41. B. Gantenbein, A.S. Croft, M. Larraillet, Mammalian Cell Viability Methods in 3D Scaffolds for Tissue Engineering, in: N. Grigoryeva (Eds.), Fluorescence Methods for Investigation of Living Cells and Microorganisms, 1st ed., Intech Open, London, 2020: pp. 1-25.